Front. Earth Sci. 2024, 18(1): 98–111
https://doi.org/10.1007/s11707-022-1048-4

RESEARCH ARTICLE

Large eddy simulation of flow over a three-dimensional hill with different slope angles

Liang LI[1], Deqian ZHENG (✉)[1,2,3], Guixiang CHEN[1,2,3], Pingzhi FANG[4], Wenyong MA[5], Shengming TANG[4]

1 School of Civil Engineering, Henan University of Technology, Zhengzhou 450001, China
2 Henan International Joint Laboratory of Modern Green Ecological Storage System, Zhengzhou 450001, China
3 Henan Key Laboratory of Grain Storage Facility and Safety, Zhengzhou 450001, China
4 Shanghai Typhoon Institute of China Meteorological Administration, Shanghai 200030, China
5 Wind Engineering Research Center, Shijiazhuang Tiedao University, Shijiazhuang 050043, China

Abstract Slope variation will significantly affect the characteristics of the wind field around a hill. This paper conducts a large-eddy simulation (LES) on an ideal 3D hill to study the impact of slope on wind field properties. Eight slopes ranging from 10° to 45° at 5° intervals are considered, which covers most conventional hill slopes. The inflow turbulence for the LES is generated by adopting a modified generation method that combines the equilibrium boundary conditions with the Fluent inherent vortex method to improve the simulation accuracy. The time-averaged flow field and the instantaneous vortex structure under the eight slopes are comparatively analyzed. The accuracy of the present method is verified by comparison with experimental data. The slope can affect both the mean and fluctuating wind flow fields around the 3D hill, especially on the hilltop and the leeward side, where a critical slope of 25° can be observed. The fluctuating wind speeds at the tops of steep hills (with slope angles beyond 25°) decrease with increasing slope, while the opposite phenomenon occurs on gentle hills. With increasing slope, the energy of the high-speed descending airflow is enhanced and pushes the separated flow closer to the hill surface, resulting in increased wind speed near the wall boundary on the leeward side and inhibiting the development of turbulence. The vortex shedding trajectory in the wake region becomes wider and longer, suppressing the growth of the mean wind near the wall boundary and enhancing the turbulence intensity.

Keywords large eddy simulation, inflow turbulence, topographic wind field, critical slope, flow mechanism

Received October 7, 2022; accepted February 6, 2023

E-mail: deqianzheng@haut.edu.cn

1 Introduction

The western mountainous areas of China are affluent in wind energy and sunlight resources, which are suitable for producing clean energy by photovoltaic arrays and wind turbines. Unlike flat terrain, predicting the wind speed in mountains is complicated due to factors such as airlift, terrain acceleration effect, turbulence intermittency, flow separation and reattachment (Yang et al., 2020). The change in hilly terrain slope significantly impacts the wind speed and flow direction of the near-ground wind field on the hillside, resulting in instability of the photovoltaic panel array on the hillside surface (Yang et al., 2021). In addition, the output of wind power is proportional to the cube of the wind speed, and the dynamic response of wind turbines is more sensitive to the turbulent wind field. It is essential to study the mean wind speed and turbulence characteristics of the terrain wind field in complex mountainous areas for the efficient site selection, design, and maintenance of photovoltaic arrays and wind farms (Uchida, 2018; Huang et al., 2019; He et al., 2020).

Generally, research on the wind field characteristics of mountainous terrain can be classified into two main categories: basic research on ideal simplified mountainous terrain and applied research on real complex mountainous terrain. Indeed, investigating the terrain wind field characteristics of ideal simplified mountains will help researchers better understand the turbulence development and vortex structure characteristics of complex terrains (Yang et al., 2021). The available approaches to study the airflow around an isolated hill are mainly theoretical analyses, wind tunnel tests and numerical simulations. The earliest approach to investigating isolated hills is the theoretical analysis

method, which can be roughly divided into two stages (Wood, 2000). In the first stage, research focused on the inviscid stage of mountain terrain under stably stratified flow (Wurtele et al., 1996). In the second stage (after 1960), the utilization of numerical models such as the perturbation method combined with the magnitude analysis of the Navier–Stokes equation was initiated. In addition, multiple linear mathematical models were proposed for predicting the mean wind and turbulent shear stress around a gentle-sloped (slope less than 20°) two-dimensional ridge (Jackson and Hunt, 1975; Hunt et al., 1988). In this stage, researchers found that the airflow around the two-dimensional ridge can be distinguished and described according to the magnitude of turbulent shear stress. Additionally, they utilized a numerical model to describe the characteristics of the maximum acceleration ratio of a single mountain without flow separation. Based on the two-dimensional ridge flow stratification concept, it was found that the boundary conditions are more reasonably imposed by adding the near-wall layer. In addition, it was highlighted that the second-order closure model simulates Reynolds stress, thus calculating the differential pressure resistance of isolated hills (Sykes, 1980). To study the influence of hill surface roughness, researchers have extended the linear mathematical model to analyze the atmospheric boundary layer flow around gentle-sloped hills with rough surfaces based on the framework proposed by Hunt (Hunt et al., 1988; Finnigan and Belcher, 2004). Although the linear mathematical models can describe the flow characteristics over gentle-sloped hills, they are inapplicable to steep-sloped hills where the linear theory fails. As a result, researchers have proposed nonlinear mathematical models to describe the wake flow of steep hills by adding the original nonlinear term into the governing equation and solving it iteratively in the spectral domain (Xu and Taylor, 1992; Wood and Mason, 1993; Hewer, 1998).

Wind tunnel tests are another widely adopted method to investigate wind flow characteristics and clarify complex flow mechanisms in mountainous terrain. Through wind tunnel tests on an ideal simplified mountain terrain such as a two-dimensional hillside or ridge or a three-dimensional hill, researchers have found that there is a pronounced acceleration effect on the mountain surface compared with the flat ground (Debray, 1973; Ishihara et al., 1999; Kondo et al., 2002). Moreover, there is an evident phenomenon of flow reattachment, which affects the development of turbulence in the wake region on the leeward side of a steep mountain (Pearse et al., 1981; Ishihara et al., 2001). Generally, the recirculation bubble on the leeward side is significantly enlarged with the increase in hill slope (Ferreira et al., 1995; Kim et al., 1997). The topography-induced acceleration effects are strengthened with the augmentation of the hill slope (Cao et al., 2012). Investigations of the dimensional effect have found that the three-dimensional hill disturbance to the flow field is weaker and that the wind speed at the top is lower than that of the two-dimensional ridge. In addition, under the influence of the flow around the leeward side, the wake intersection on the leeward side results in a small cavity area, and the secondary flow effect causes the attenuation of the turbulent fluctuating velocity in the wake region of the three-dimensional hill (Gong and Ibbetson, 1989; Ishihara et al., 2001; Flay et al., 2019). Moreover, due to the influence of mountain roughness, the turbulent mixing effect leads to the formation of the terrain internal boundary layer, which significantly increases the terrain acceleration effect at the top of the hill, resulting in a remarkable separation bubble on the leeward side and a long reattachment length of the separated airflow (Takahashi et al., 2002).

With the development of turbulence models, numerical simulation has been widely adopted to evaluate the wind field characteristics around mountains. The Reynolds-averaged Navier–Stokes (RANS) and spatially averaged large eddy simulation (LES) methods are two common numerical simulation methods (Hu et al., 2016; Fang et al., 2019). For the RANS method, previous studies have found that the standard k-ε model can accurately predict the flow field of a gentle mountain without flow separation, but the prediction accuracy is insufficient in the case of the leeward side of a steep mountain (Ishihara and Hibi, 2000; Kim et al., 2001; de Mello and Yanagihara, 2010). Ferreira et al. (1995) improved the prediction accuracy of the standard k-ε model with a low Reynolds number. Loureiro et al. (2008) compared six different RANS models and found that the turbulence model based on the ω equation can predict the mean wind speed, wall shear stress, and the length of separation and reattachment in the wake region of a two-dimensional steep ridge. Nevertheless, it is difficult to simulate the fluctuating wind flow, capture the instantaneous vortex structure and the significant flow separation effect on the leeward side of steep mountains by RANS. In contrast, large eddy simulation has the advantage of capturing the instantaneous vortex structure and turbulent flow field (Tamura, 2008). By large eddy simulation of flow around a two-dimensional ridge based on different subgrid-scale models, researchers found that the scale similarity model-based results possess the highest simulation accuracy (Iizuka and Kondo, 2004). Further research implies that the turbulent wind field of two-dimensional steep ridges and three-dimensional steep hills, with smooth or rough surfaces or covered by vegetation, can be accurately simulated employing the dynamic Smagorinsky model or the coherent structure Smagorinsky model. Moreover, roughness plays a significant role in the hill turbulent flow field and affects the size of the backflow area on the leeward side (Cao et al., 2012; Yang et al., 2021).

Previous studies indicate that the surface roughness, shape and slope of the hill can impact the flow pattern

and the development of turbulent flow around the hill (Cao et al., 2012; Liu et al., 2016; Yang et al., 2021). In particular, the slope variation can significantly affect the development of the turbulence flow around the hill, influencing the construction and maintenance of vortex structures on the leeward side. Nevertheless, most studies considered no more than four slopes (Tamura et al., 2007; Yang et al., 2021). Systematic research is still lacking on the slope effect and mechanism on the wind flow field around hilly terrain, especially on the development of turbulence structure in the wake region. By using an ideal three-dimensional hill as the research object, unsteady flow around the hill was numerically calculated by adopting the LES method on the Ansys Fluent 14.5 commercial code. The inflow turbulence for LES was generated by combining the equilibrium boundary conditions (Yang et al., 2009) with the Fluent inherent vortex method (Mathey et al., 2006) to improve the simulation accuracy. The effectiveness of this numerical simulation method was verified by comparing the LES results of a three-dimensional hill with a slope of 21.8° to those of the corresponding wind tunnel test (Liu et al., 2016). The influence of the slope on the mean and fluctuating wind profiles at different positions of the hill was investigated in detail, considering eight slopes: 10°, 15°, 21.8°, 25°, 30°, 35°, 40°, and 45°. The corresponding mechanism of the wind flow field, especially on the leeward side, was analyzed from the perspective of time-averaged and instantaneous flow fields.

2 Numerical simulation method for LES

2.1 Governing equations

Large eddy simulation was first proposed by Smagorinsky (1963) and uses a filter function to separate large-scale eddies from small-scale eddies. The separated large-scale eddies are directly solved, while the small-scale eddies are simulated by a turbulence model. The governing equations for large eddy simulation are

$$\frac{\partial \overline{u}_i}{\partial x_i} = 0, \tag{1}$$

$$\frac{\partial \overline{u}_i}{\partial t} + \frac{\partial \overline{u}_i \overline{u}_j}{\partial x_j} = -\frac{1}{\rho}\frac{\partial \overline{p}}{\partial x_i} + v\frac{\partial^2 \overline{p}}{\partial x_j \partial x_j} - \frac{\partial \overline{\tau}_{ij}}{\partial x_j}, \tag{2}$$

where $\overline{u}_i$ and $\overline{u}_j$ are the filtered velocity, ρ is the fluid density, $\overline{p}$ is the filtered pressure, v is the hydrodynamic viscosity, and τ_{ij} is the subgrid-scale (SGS) stress (required to establish a corresponding model to satisfy the equations). This paper employs the dynamic SGS model (Germano et al., 1991; Lilly, 1992), which can be represented as follows:

$$\tau_{ij} - \frac{1}{3}\tau_{kk}\delta_{ij} = -2u_t \overline{s}_{ij}, \tag{3}$$

$$\overline{s}_{ij} = \frac{1}{2}\left(\frac{\partial \overline{u}_i}{\partial x_j} + \frac{\partial \overline{u}_j}{\partial x_i}\right), \tag{4}$$

where $\overline{s}_{ij}$ is the rate-of-strain tensor for the resolved scale, δ_{ij} is the Kronecker delta, and μ_t is the SGS turbulent viscosity, which is described as follows:

$$\mu_t = \rho l_s^2 |\overline{s}|, \tag{5}$$

where l_s is the mixing length for subgrid scales. The value of l_s is determined by the minimum of κd and $c_s V^{\frac{1}{3}}$, in which κ is the von Karman constant, d is the distance to the nearest wall and V is the volume of a computational cell. c_s is the Smagorinsky constant, which is dynamically provided to better simulate the collision, separation, free shear layer, and vortex shedding in the flow field around the bluff body.

2.2 Modified inflow turbulence generation method

The inflow turbulence plays a significant role in the large eddy simulation of wind flow around hilly terrains in the atmospheric boundary layer. In this study, a modified inflow turbulence generation method was proposed by combining the equilibrium boundary conditions (Yang et al., 2009) with the Fluent inherent vortex method (Mathey et al., 2006) to improve the simulation accuracy. The inflow turbulence was generated by adding the fluctuating velocities to the specified mean wind speed profile. The mean wind profile adopted here is defined by the logarithmic law as follows (Tamura, 2008):

$$U(z) = \frac{u^*}{\kappa}\ln\left(\frac{z+z_0}{z_0}\right), \tag{6}$$

where κ is the von Karman constant (0.42), u^* is the friction velocity, and z_0 is the roughness height, as listed in Table 1.

The fluctuating wind speed was generated by constructing a randomly distributed two-dimensional vorticity field on the inflow panel of the computational domain. The characteristic scale of the local vortex was related to the turbulent kinetic energy and turbulent dissipation rate at the inflow boundary. A simplified linear kinematics model was then applied to describe the turbulent fluctuation along the flow direction of the domain. The vortex method has a similar advantage in parallel processing as the prevailing inflow turbulence generation method (e.g., the MDSRFG by Castro and Paz

Table 1 Fitting values of wind farm parameters

Parameters	u^*/(m·s^{-1})	z_0/m	C_1	C_2
Fitted values	0.511	0.000225	−0.41889	0.42874

(2013), the DSRFG by Aboshosha et al. (2015), and the NSRFG by Yu et al. (2018)). The fluctuating wind velocities at the inflow boundary are mainly synthesized as follows (Mathey et al., 2006):

$$\vec{u}\left(\vec{x}\right)=\frac{1}{2\pi}\sum_{i=1}^{N}4\sqrt{\frac{\pi S k(x,y)}{3N(2\ln 3-3\ln 2)}}\frac{\left(\vec{x_i}-\vec{x}\right)\times\vec{z}}{\left|\vec{x}-\vec{x_i}\right|^2}\cdot\left(1-\mathrm{e}^{-\frac{\left|\vec{x}-\vec{x_i}\right|^2}{2\sigma^2}}\right)\mathrm{e}^{-\frac{\left|\vec{x}-\vec{x_i}\right|^2}{2\sigma^2}},\tag{7}$$

where N is the number of vortex points, S is the area of the model inlet boundary, k is the turbulent kinetic energy, $\vec{x}$ is the two-dimensional coordinate of each vortex, $\vec{x_i}$ is the two-dimensional coordinate of each vortex center, $\vec{z}$ is the unit vector in the streamwise direction, and σ is the characteristic scale of the vortex defined by

$$\sigma=\frac{ck^{3/2}}{2\varepsilon},\tag{8}$$

where $c=C_\mu^{3/4}$ with $C_\mu=0.09$.

Equation (8) above indicates that the characteristic scales of the vortex are dominated by the profile of the turbulent kinetic energy and the rate of dissipation. In practice, the initial flow field for LES is generally obtained from a fully developed flow field by a steady-state RANS calculation. The equilibrium boundary condition, proposed by Yang et al. (2009), possesses the advantage of maintaining a profile for approaching wind flow, which is essential for RANS calculation. Thus, it was introduced in this study for combination with the Fluent inherent vortex method. Expressions of the equilibrium boundary condition include the mean wind profile of Eq. (6), and the turbulent kinetic energy k and the dissipation rate ε as

$$k(z)=\sqrt{2C_1\ln(z+z_0)z+C_2},\tag{9}$$

$$\varepsilon=C_\mu^{1/2}k(z)\frac{\partial u}{\partial z},\tag{10}$$

where C_1 and C_2 are constants (listed in Table 1).

As a comparison to verify the efficacy of the combined equilibrium boundary conditions, expressions of the conventional inflow boundary condition, namely, the nonequilibrium boundary conditions, are also considered. The mean wind velocity is the same as that in Eq. (6), whereas the turbulent kinetic energy k and dissipation rate ε are as follows (Sagrado et al., 2002):

$$k=\frac{3}{2}(UI_u)^2,\tag{11}$$

$$\varepsilon=C_\mu^{\frac{3}{4}}k^{\frac{3}{2}}/\kappa z,\tag{12}$$

where U is the mean wind profile and I_u is the turbulence intensity (Zheng et al., 2012).

$$I_u=\begin{cases}c_1-c_2\ln(z+z_0), & z_0\geqslant 0.035\\ 5.71(z+z_0), & z_0\leqslant 0.035\end{cases},\tag{13}$$

where c_1 and c_2 are the constants to be fitted.

2.3 Computational domain and parameter settings

The ideal three-dimensional hill depicted in Fig. 1 is a cosine 3D symmetric hill:

$$z_s(x,y)=\begin{cases}H\cos^2\left(\dfrac{\pi\left(x^2+y^2\right)^{1/2}}{2L}\right), & \left(x^2+y^2\right)^{1/2}<L\\ 0, & \left(x^2+y^2\right)^{1/2}\geqslant L\end{cases},\tag{14}$$

where L is the horizontal length of the windward or leeward side of a 3D hill, determined to be a constant equal to 1000 mm.

The hill slope was defined as $\tan\alpha = H/L$, where α = 10°, 15°, 21.8° (verification model), 25°, 30°, 35°, 40°, and 45°, by varying the height H of the 3D hill. The geometric scale ratio of the model is 1:500, and the hill has a type B ground roughness (with a power law index of 0.15 for the mean velocity profile), according to the

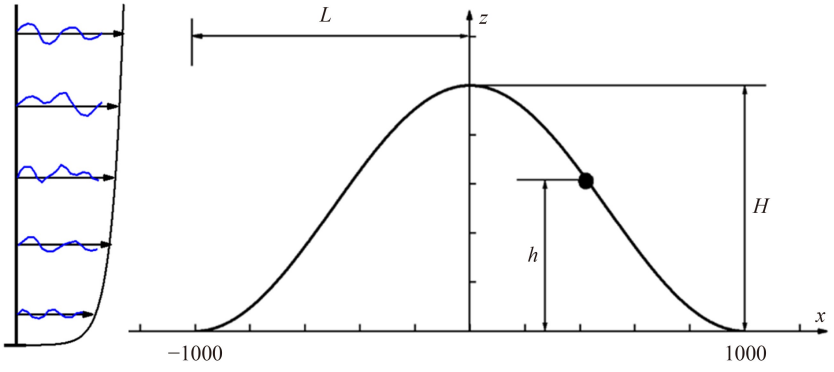

Fig. 1 Schematic diagram of the mountain shape.

Chinese Load Code (Load code for the design (GB 5009-2012), 2012).

The computation domain was set as $23L(x) \times 6L(y) \times 6L(z)$ with a blocking ratio below 3.0%, as shown in Fig. 2, where the boundary settings were given. A nonuniform structured grid (Fig. 3) was utilized to discretize the computational domain, in which the grid was refined near the wall boundary. Two kinds of meshes (namely, Mesh-1 and Mesh-2) were considered to obtain the grid independence solution in the verification of the present simulation method. The main grid parameters are summarized in Table 2. The nondimensionalized first grid points near the wall boundary, i.e., the corresponding wall unit y^+, were both less than 5.5.

The inflow turbulence was generated by using the present synthesis method, which combines the Fluent inherent vortex method with the equilibrium boundary conditions discussed in Section 2.2. In addition, the nonequilibrium expression combined method was also considered for comparison. The initial values for LES were obtained by steady-state RANS calculation. The pressure-velocity decoupling method utilizes the SIMPLEC algorithm. Discretization for the convective terms of momentum equations was the bounded central differencing scheme. The time discretization scheme was second-order implicit with a time-step size of 0.0004 s. For the two meshes, approximately 92% of the grid courant numbers were less than 1.0, indicating that the time step and grid size described in this paper satisfied the CFL (Courant–Friedrichs–Lewy) conditions. The SGS model chosen in this study was the Dynamic Smagorinsky-Lilly model (Germano et al., 1991; Lilly, 1992).

3 Verification of the present simulation method

To verify the performance of the present numerical simulation method and parameter settings, the LES results of a 3D hill with a slope of 21.8° were first compared to the experimental results (Liu et al., 2016) in terms of the simulated approaching wind profiles and the flow field over the hill model.

In the following analysis, U is the flow direction mean wind speed, U_{ref} is the average mean wind speed of the incoming flow direction at a height of $4H$ above the ground, and I_u is the turbulence intensity (defined as I_u =

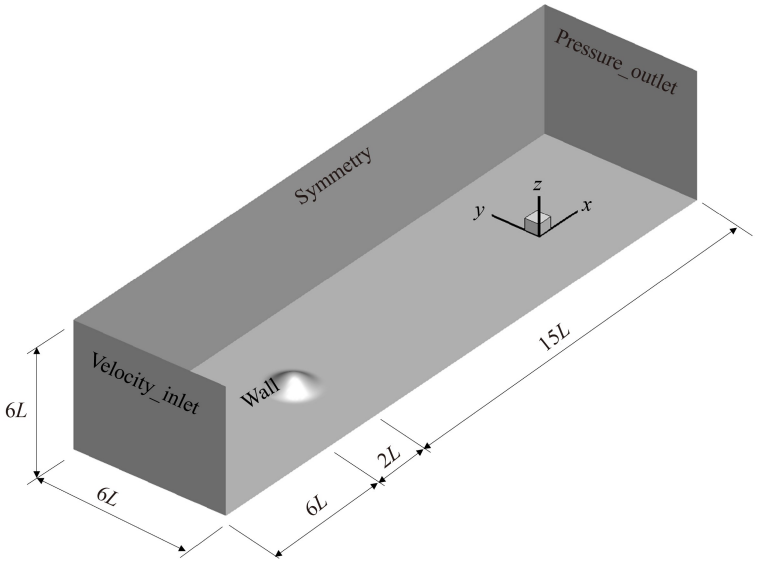

Fig. 2 Computational domain of the numerical model.

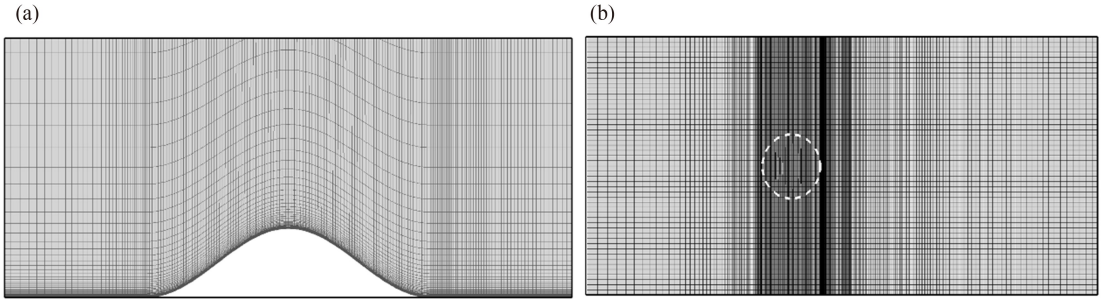

Fig. 3 Mesh distributions of the numerical model: (a) vertical plane grid and (b) horizontal plane grid.

Table 2 Grid resolution

Case	Computational domain	Total number of grids	Minimum mesh size
kfit_Mesh-1	$23L(x) \times 6L(y) \times 6L(z)$	976500	$0.0003L$
kfit_Mesh-2	$23L(x) \times 6L(y) \times 6L(z)$	1904000	$0.0001L$
Iufit_Mesh-1	$23L(x) \times 6L(y) \times 6L(z)$	976500	$0.0003L$

Notes: kfit: self-retaining boundary conditions; Iufit: non-self-retaining boundary conditions.

σ_u/U), in which σ_u is the fluctuating wind speed in the flow direction and L_u is the integral length scale of streamwise turbulence.

3.1 Validation of the simulated turbulence boundary layer

Figure 4 compares the profiles of the mean wind velocity and turbulence intensity of the LES located $2.5L$ in front of the foot of a 3D hill on the windward side under various grid resolutions with a wind tunnel test (Liu et al., 2016), as well as the fluctuating wind speed spectrum at height H from the ground and the Von Karman spectrum. The "kfit" and "Iufit" in the legend represent the LES results of the equilibrium and nonequilibrium boundary condition-based vortex method, respectively, defined in Section 2.2. "Mesh-1" and "Mesh-2" are the two mesh schemes, as listed in Table 2.

For the performance of the equilibrium boundary condition-based vortex method (i.e., the present modified generation method), the mean wind velocity and turbulence profile of the two meshes (Fig. 4(a)) are precisely regenerated, and good agreement is achieved. Moreover, as illustrated in Fig. 4(b), the fluctuating wind speed spectra agree with the Von Karman spectra at low frequencies. Despite a certain attenuation at higher frequencies due to the grid filtering effect, it can reflect the energy distribution of the inertial subarea and satisfy engineering application needs. No significant difference can be observed for the two meshes when adopting the present modified generation method. In contrast, a remarkable discrepancy in the fluctuating wind speed spectrum is observed when adopting the nonequilibrium-based vortex method.

3.2 Verification of the LES results of the wind flow field around the hill

Figure 5(a) depicts the simulated mean wind profiles in the streamwise direction at several locations from $x = -2.5H$ to $x = 6.25H$ for the two grid resolutions. The numerical results obtained by LES at various locations agree with the experimental measurements. There is no significant difference between the results of the two resolution grids, indicating that increasing the grid resolution does not significantly improve the simulation accuracy of the mean wind profiles. On the windward side, the mean wind profiles reveal an evident acceleration on the hill surface, and the largest acceleration effects are manifested at the crest. After the crest, the 3D hill disturbs the high-speed airflow, creating a flow separation in the leeward area (Fig. 9(c)) and a reverse point where the flow direction changes from positive to negative as it approaches the surface at $x/H = 1.25$. The region of the separation bubble starts at $x/H = 0.91$ and ends at $x/H = 2.5$, which is similar to the findings from Ishihara et al. (2001).

Accurate simulation of the development of turbulence is critical to reproducing the characteristics of the wind field around a 3D hill. The simulated turbulence intensity profiles over the hill are shown in Fig. 5(b), and the simulation results agree with the wind tunnel test trend (Liu et al., 2016). The simulated turbulence intensity

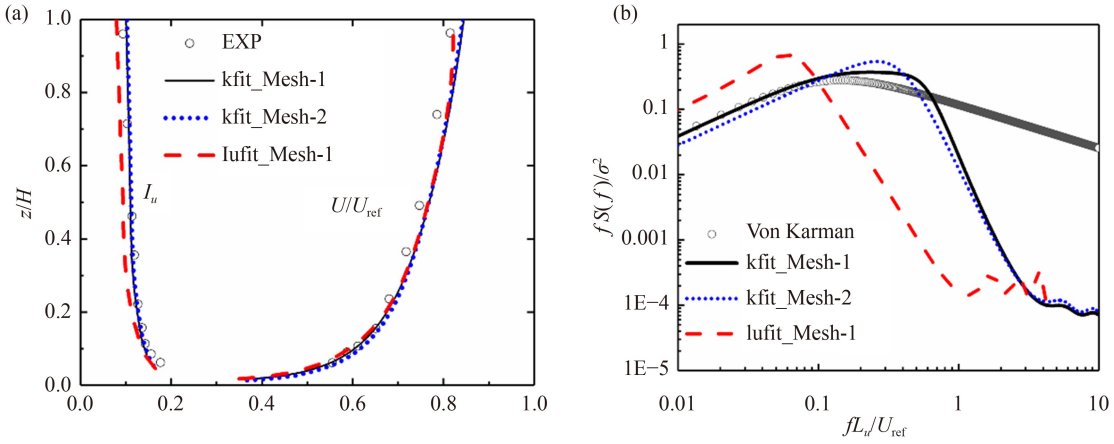

Fig. 4 Comparisons of (a) normalized mean velocity and turbulence intensity profiles and (b) fluctuating wind speed spectrum.

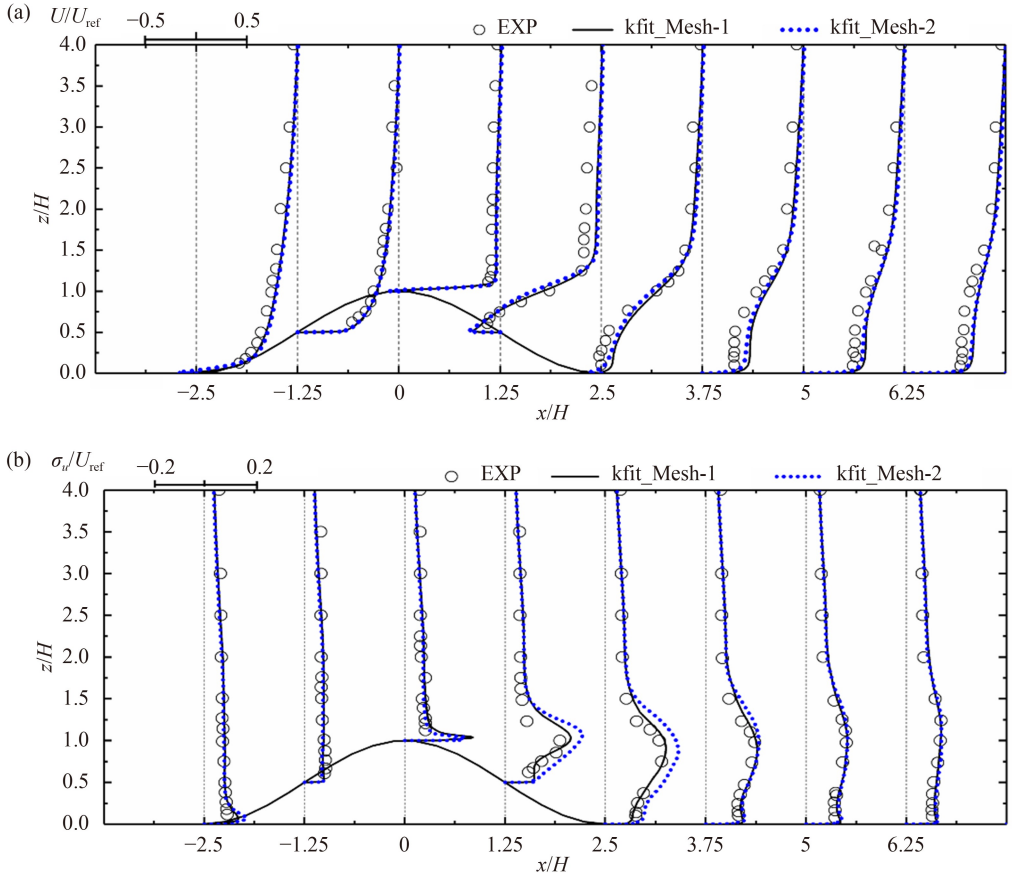

Fig. 5 Comparisons of the mean wind profiles (a) and turbulence intensity profiles (b) between results of large eddy simulation and wind tunnel test.

profiles under the two grid resolutions are accurately rebuilt on the windward side to the crest. The differences from the experimental measurements are mainly concentrated from positions $x/H = 1.25$ to $x/H = 3.75$. The value of the streamwise turbulence intensity simulated by Mesh_2 (Fig. 5(b)) is slightly higher than the test value, but the error between that and the wind tunnel test is less than 5.0%. In general, the simulated results by LES of the two sets of grids can reflect the variation trend of fluctuating wind speed around the hill and its wake flow field.

The above comparison results indicate that the present inflow turbulence generation method and parameters for large eddy simulation are capable of precisely reproducing both the approaching turbulence boundary layer and the characteristics of the wind flow field around 3D hilly terrain. The following analysis of the impact of slope on a 3D hill wind field is based on the kfit_Mesh-1 case according to the large eddy simulation accuracy and calculation efficiency.

4 Effect of slope angles on wind profiles over the hill

Based on the verified simulation method and parameter settings, large eddy simulation of unsteady flow around the 3D hill is conducted on eight slopes ranging from 10° to 45° at 5° intervals, which covers most conventional hill slopes. In this section, the influence of slope angle on the flow field over the 3D hill is comparatively analyzed in terms of the mean and fluctuating wind profiles in the streamwise direction at typical measurement points, as shown in Fig. 6. The mean flow field and the instantaneous vortex structure are also discussed to study the influence mechanism.

4.1 Effect on the mean wind profiles

Comparisons of the mean wind profiles under the eight slopes are shown in Fig. 7, where $z' = z_i - h_i$ and the

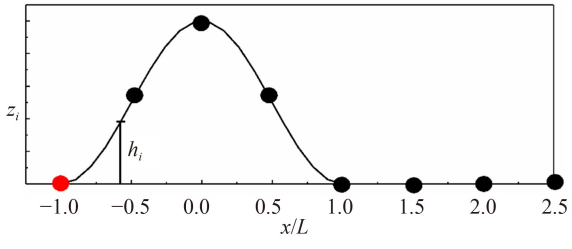

Fig. 6 Schematic diagram of the measurement point locations.

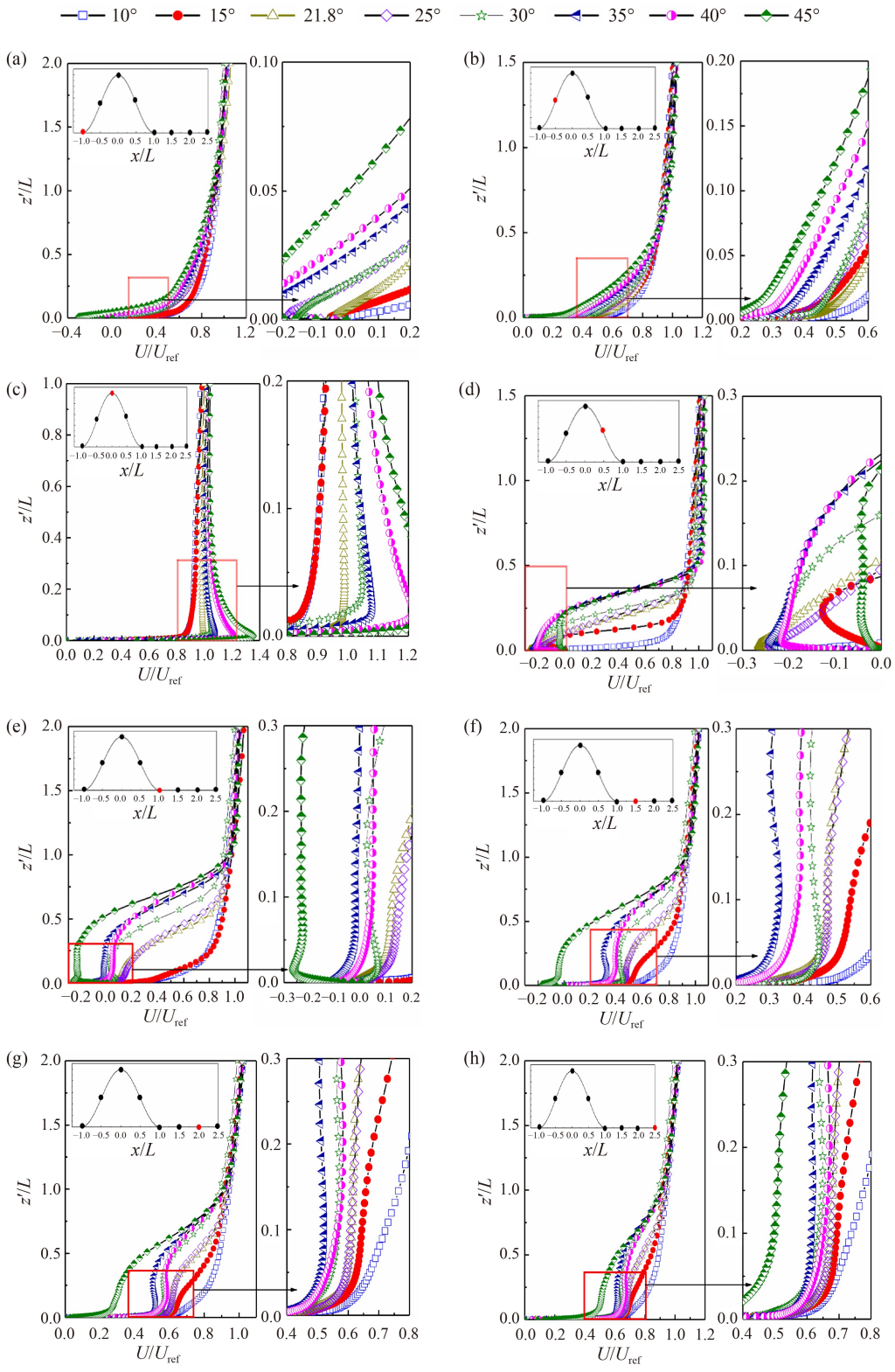

Fig. 7 Profiles of the normalized mean velocities for the flow over 3D hill at different slopes. (a) $x/L = -1.0$, (b) $x/L = -0.5$, (c) $x/L = 0$, (d) $x/L = 0.5$, (e) $x/L = 1.0$, (f) $x/L = -1.5$, (g) $x/L = 2.0$, and (h) $x/L = 2.5$.

definitions of z_i and h_i are shown in Fig. 6. The variation trend of the mean wind profiles with many slopes on the windward side is identical, e.g., Figs. 7(a), 7(b), and 7(c), and the wind speed rises as the height of the measuring point increases. Blocked by the mountain, the reverse flow phenomenon occurs at the foot of the mountain on the windward side and forms a standing vortex (Fig. 9), causing a sudden change in the mean wind profiles. With

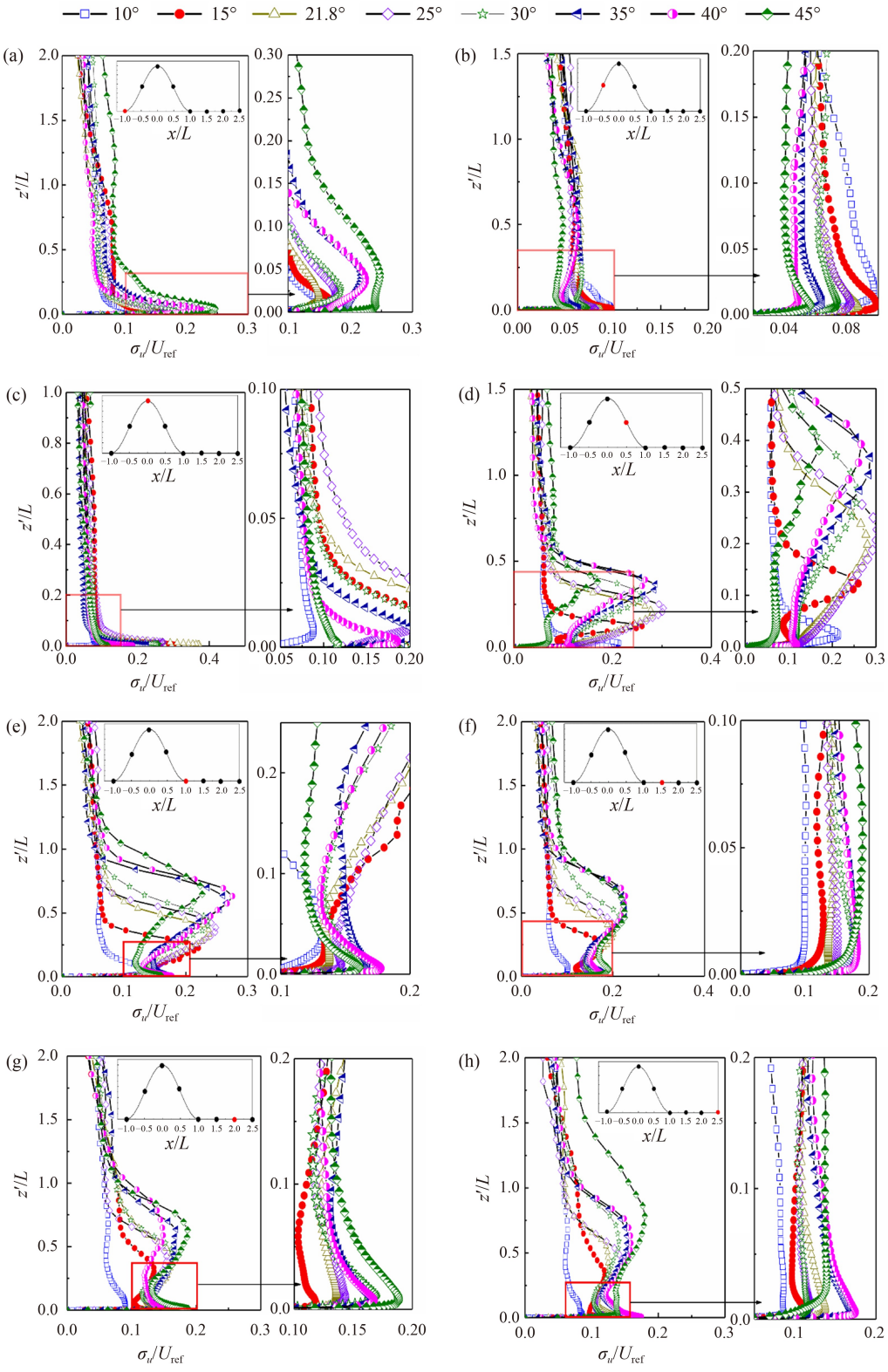

Fig. 8 Profiles of the normalized fluctuating wind velocities for the flow over 3D hill at different slopes. (a) $x/L = -1.0$, (b) $x/L = -0.5$, (c) $x/L = 0$, (d) $x/L = 0.5$, (e) $x/L = 1.0$, (f) $x/L = -1.5$, (g) $x/L = 2.0$, and (h) $x/L = 2.5$.

the increase in slope, the terrain acceleration effect of the wind flow field gradually increases and reaches its maximum at the top of the mountain, where the largest wind speed of the 45° slope model is approximately 41.4% higher than that on the ground. In the leeward region, high-speed airflow impacts the ground and the mountain surface, resulting in a reverse flow phenomenon, forming a vortex on the leeward side (Fig. 9) and

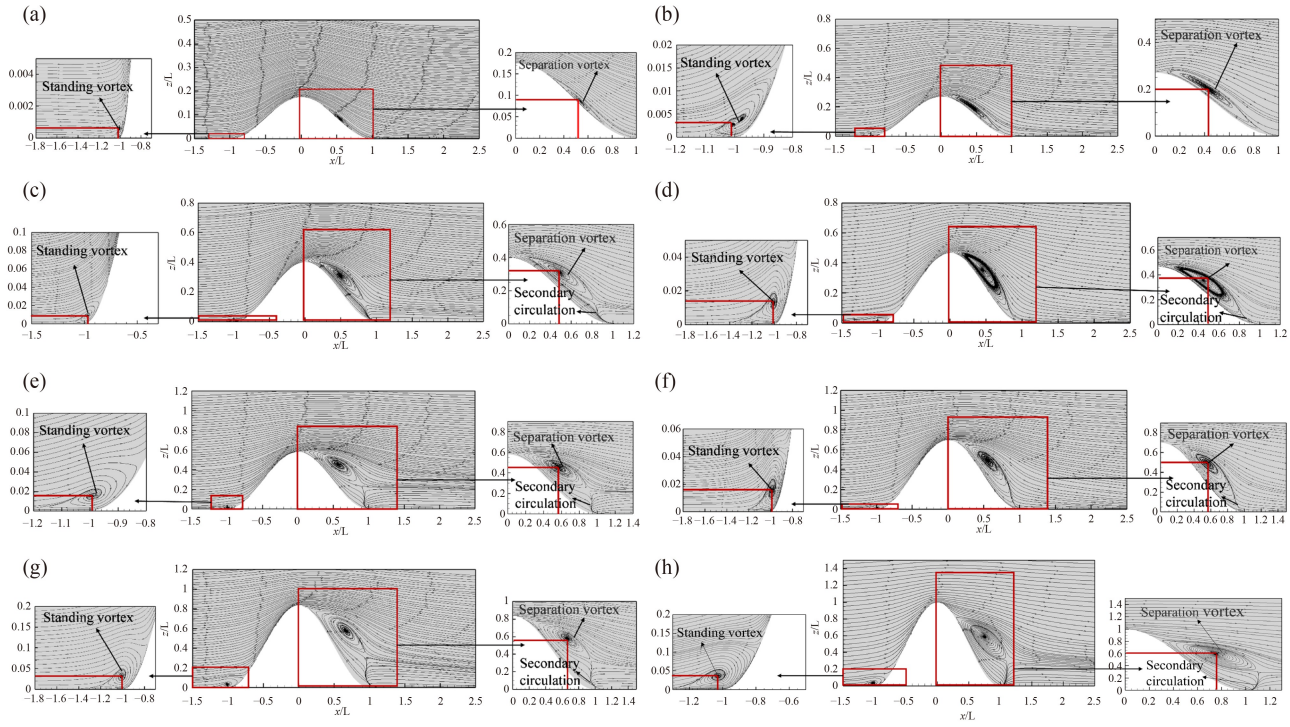

Fig. 9 Time-averaged streamline of three-dimensional hills with different slopes. (a) 10°, (b) 15°, (c) 21.8°, (d) 25°, (e) 30°, (f) 35°, (g) 40°, and (h) 45° on the longitudinal section of $y = 0$.

causing a gradual decrease in the mean wind velocity. The vortex on the leeward side slowly rises as the slope increases, and the reverse flow phenomenon at the foot of the hill pushes the vortex away from the wall and close to the downstream, resulting in an upward trend in the mean wind profiles when the slope is greater than 21.8°. In the wake region, the near-wall wind speed gradually decreases with increasing slope; moreover, the influence range of the secondary circulation (Fig. 9) continues to expand, resulting in an abrupt change in the wind speed of the steep hillside near the wall of the wake area.

4.2 Effect on the fluctuating wind profiles

Figure 8 depicts comparisons of the fluctuating wind profiles in the streamwise direction at different slopes. At the foot of the mountain on the windward side (Fig. 8(a)), the fluctuating wind profiles present a gradual increase with slope since the standing vortex size grows (as shown in Fig. 9) and the energy becomes correspondingly concentrated with the increase in slope. On the leeward side and in the wake region, multiscale vortices generated by flow separation from the top and the two sides of the hill are mixed together (Fig. 10), and the flow becomes more complicated and highly turbulent. Thus, the shape of the fluctuating wind profile deforms over a wide height range, and the influenced height above the hill surface can reach up to $z'/L = 1.0$ when $x/L \geqslant 0.5$ (Figs. 8(d)–8(h)). In addition, the fluctuating wind velocities also increase significantly, and the greatest increase occurs at $x/L = 0.5$, as shown in Fig. 8(d).

At the hilltop of $x/L = 0$ (Fig. 8(c)), fluctuation of the wind flow near the mountain surface is mainly dominated by flow separation. With increasing slope, the blocking effect of the hill on the incoming airflow becomes remarkable. When the hill slopes are gentle ($\alpha \leqslant 25°$), the blocking effect is not apparent. As a result, the fluctuating wind speed near the wall at the top of the hill (Fig. 8(c)) is gradually enlarged as the slope increases. In contrast, when the slope of the hill is steep ($\alpha > 25°$), the blocking effect of the mountain height on the incoming wind speed slowly grows, and the ascending airflow along the windward side of the mountain consumes the airflow energy along the windward side of the mountain; therefore, the fluctuating wind speed near the surface of the hilltop (Fig. 8(c)) gradually decreases with increasing slope.

At the hillside and foot of the hill on the leeward side (Figs. 8(d) and 8(e)), affected by the separation of the airflow on the leeward side and the shielding effect of the height of the hill, the high-speed descending air converges with the flow around both sides of the hill, complicating the variation in the fluctuating wind velocity within this region. The fluctuating wind profile near the hill surface rises with increasing slope when the slope is less than 25°, while it drops with increasing slope when the slope is greater than 25°.

4.3 Time-averaged flow field

Figure 9 depicts the time-averaged streamline of the 3D hill along the longitudinal section of $y = 0$ with different

slopes. Due to the blocking effect by the mountain, a reversed flow with a standing vortex is formed at the foot of the windward side. The emergence of a standing vortex reduces the wind speed in the streamwise direction. With the increase in slope, the reversed flow region and the standing vortex size are enlarged, inducing energy concentration and enhancing fluctuation of the wind speed. The wind speed at the hilltop gradually increases with slope, and the flow separation point position moves downward correspondingly.

On the leeward side, large-scale eddies are generated by flow separation, accompanied by vortex shedding phenomena (Fig. 10). With increasing slope, the size and range of the vortex increase gradually, and the vortex core coordinates of the eight slope hills are listed in Table 3. For the gentle 10° slope, the separation bubble on the leeward side is close to the ridge line. However, with the increase in the slope, the vortex core gradually moves down and away from the hill surface, which is caused by the higher wind speed in the near wall region at the top of the steep hill (Fig. 7(c)). For the steep hill, the increase in the separation bubble range also decreases the fluctuating wind velocity near the hill surface (Fig. 8(d)). Moreover, the high-speed downward developing airflow converges with the airflow on both sides of the hill, inducing more prominent formation of the secondary circulation at the foot of the mountain on the leeward side. As the slope increases, the secondary circulation influencing range also increases gradually, resulting in a slow decrease in the wind speed in the wake region. With the expansion of the influence range of the secondary circulation, the large-scale eddies and the corresponding energy are more concentrated in this range, causing the fluctuating wind speed to grow with increasing slope.

Table 3 Vortex core coordinates

Model	x/L	z/L
10°	0.54	0.19
15°	0.44	0.2
21.8°	0.49	0.32
25°	0.5	0.38
30°	0.55	0.45
35°	0.58	0.5
40°	0.65	0.55
45°	0.75	0.6

4.4 Instantaneous vortex structure

The instantaneous vortex structure, depicted by the Q criterion (Hunt et al., 1988), is employed to study the turbulent flow field around the hill. Figure 10 shows the vortex distribution around the hill of different slopes under $Q = 1000$ with the same calculation time step of $t =$ 24 s.

Blocked by the hill, horseshoe vortices are observed in front of the hill. As the slope increases, the horseshoe vortex becomes remarkable, increasing the energy concentration and intensifying the fluid turbulence. The scale of the horseshoe vortex enlarges with an increasing slope. As the horseshoe vortices accumulate, they move to both sides of the hill and gradually develop into obvious drag vortices. Vortex shedding occurs at the hilltop and on both sides as the vortex gradually evolves along the hill. An arc-type shear vortex slowly develops on the leeward surface and forms into a large-scale vortex ring. The separated vortex at the hilltop moves downward and collides with the drag vortex on both sides of the hill and those on the hill surface, gradually diminishing the

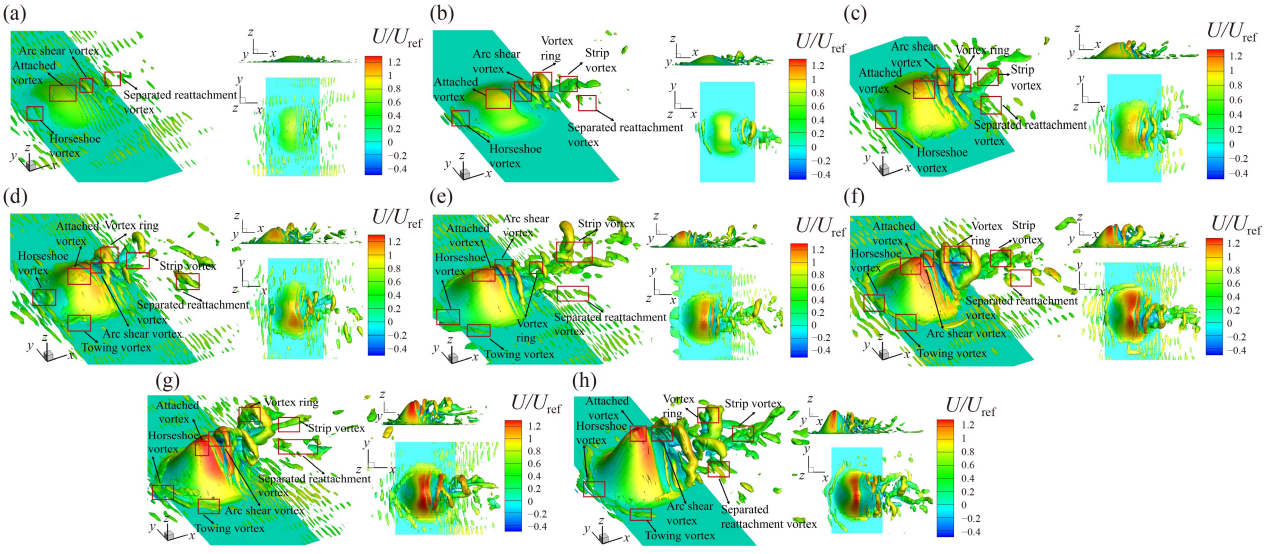

Fig. 10 Instantaneous vortex structure with $Q = 1000$ for different slopes. (a) 10°, (b) 15°, (c) 21.8°, (d) 25°, (e) 30°, (f) 35°, (g) 40°, and (h) 45°.

size of the large-scale vortex on the leeward side of the hill. As a result of the three-dimensional effect of the hill, the vortex shedding on the leeward side becomes more complicated, and energy is more dispersed as the slope increases, resulting in turbulence attenuation (Fig. 10(d)). Accompanied by the phenomenon of vortex shedding, a vortex path dominated by large-scale and alternating small-scale eddies is formed in the wake region. With increasing slope, the vortex shedding track range in the wake region increases gradually, and the vortex path is longer and wider than that of gentle hills ($\alpha \leqslant 25°$). Moreover, in the wake region, the vortex size near the wall boundary rises as the slope increases, and several small-scale eddies transform into large-scale eddies after being mixed. Above the ground, a strip vortex can be observed. The lifting effect of the ascending airflow along the steep hill causes the large-scale strip vortex to move upward, forming a spiral vortex shedding track. The scale of the strip vortex grows and runs through the entire vortex channel, making the energy in this region more concentrated and the turbulence more intense (Fig. 10(d)). At the same time, with the increase in large-scale eddies in the vortex channel, the collision phenomenon of steep hills ($\alpha > 25°$) in the wake region becomes more prominent. Affected by the airflow, part of the small-scale eddies generated by the collision move upward, causing greater energy dissipation and influencing turbulence development. Another portion of the small-scale vortex gradually descends and attaches to the ground, forming a more obvious attached vortex, which enhances the turbulence intensity of the steep hill near the ground in the wake region.

5 Conclusions

1) A modified inflow turbulence generation method for large eddy simulation was developed by combining the equilibrium boundary conditions with the Fluent inherent vortex method. By comparing the results with wind tunnel data, the present method is verified to be capable of accurately reproducing the wind profiles and wind speed spectrum of the atmospheric boundary layer, as well as predicting the characteristics of the wind field around a 3D hill, especially on the leeward side and in the wake region.

2) For the mean and fluctuating wind profiles, the influence of slope is mainly concentrated around the hill and in the wake region. The increase in slope inhibits the development of the mean wind speed near the wall boundary of the windward side but increases the wind speed at the top of the hill. On the peak and leeward sides, a critical slope of 25° exists, and the mean wind on the hillside of the leeward side gradually increases with increasing slope when $\alpha > 25°$, while the fluctuating wind gradually decreases. However, the mean wind gradually decreases with increasing slope when $\alpha \leqslant 25°$, while the fluctuating wind gradually increases. In the wake region, the mean wind near the ground gradually decreases with increasing slope, while the fluctuating wind gradually increases.

3) The increasing slope gradually increases the size of the standing vortex at the windward side of the hill, resulting in more energy accumulation and substantial turbulence. At the hilltop, the attached vortex of the steep hill ($\alpha > 25°$) rapidly develops into a shear vortex ring, which inhibits the development of turbulence at the top of the steep hill to a certain extent. Moreover, the high-speed downward flow at the top of the mountain gradually moves the separation vortex on the leeward side away from the surface of the hill and close to the downstream, and the lifting effect of the leeward flow gradually moves the steep hill ($\alpha > 25°$) away from the hill, which inhibits the development of turbulence to a certain extent and increases the wind speed near the hill surface. On the other hand, in the wake region, the vortex shedding trajectory gradually widens and lengthens with increasing slope, making the energy more concentrated and promoting the development of turbulence.

Acknowledgments This study was jointly supported by the National Key R & D Plan of China (No. 2018YFB1501104), the National Natural Science Foundation of China (Grant No. 52278511), the Natural Science Foundation of Hebei Province (No. E2021210053) and the Young Backbone Teacher Cultivation Program of Henan University of Technology.

References

Aboshosha H, Elshaer A, Bitsuamlak G T, El Damatty A (2015). Consistent inflow turbulence generator for les evaluation of wind-induced responses for tall buildings. J Wind Eng Ind Aerodyn, 142: 198–216

Cao S, Tong W, Ge Y, Tamura Y (2012). Numerical study on turbulent boundary layers over two-dimensional hills-effects of surface roughness and slope. J Wind Eng Ind Aerodyn, (104–106): 342–349

Castro H G, Paz R R (2013). A time and space correlated turbulence synthesis method for large eddy simulations. J Comput Phys, 235: 742–763

de Mello P E B, Yanagihara J I. (2010). Numerical prediction of gas concentrations and fluctuations above a triangular hill within a turbulent boundary layer. J Wind Eng Ind Aerodyn, 98(2): 113–119

Debray B G (1973). Atmospheric shear flows over ramps and escarpments. Industrial Aerodynamics Abstracts, 9: 1–4

Fang P Z, Zheng D Q, Li L, Ma W Y, Tang S M (2019). Numerical and experimental study of the aerodynamic characteristics around two-dimensional terrain with different slope angles. Front Earth Sci, 13(4): 705–720

Ferreira A D, Lopes A, Viegas D X, Sousa A (1995). Experimental and

numerical simulation of flow around two-dimensional hills. J Wind Eng Ind Aerodyn, 54(94): 173–181

Finnigan J J, Belcher S E (2004). Flow over a hill covered with a plant canopy. Q J R Meteorol Soc, 130(596): 1–29

Flay R G J, King A B, Revell M, Carpenter P, Turner R, Cenek P, Safaei Pirooz A A (2019). Wind speed measurements and predictions over belmont hill, wellington, new zealand. J Wind Eng Ind Aerodyn, 195: 104018

Garcia Sagrado A P, van Beeck J, Rambaud P, Olivari D (2002). Numerical and experimental modelling of pollutant dispersion in a street canyon. J Wind Eng Ind Aerodyn, 90(4–5): 321–339

GB 5009-2012 (2012). Load code for the design of building structures. Ministry of Construction, China (in Chinese)

Germano M, Piomelli U, Moin P, Cabot W H (1991). A dynamic subgrid scale eddy viscosity model. Phys Fluids A Fluid Dyn, 3(7): 1760–1765

Gong W, Ibbetson A (1989). A wind tunnel study of turbulent flow over model hills. Boundary-Layer Meteorol, 49(1–2): 113–148

He Y C, He J Y, Chen W C, Chan P W, Fu J Y, Li Q S (2020). Insights from Super Typhoon Mangkhut (1822) for wind engineering practices. J Wind Eng Ind Aerodyn, 203: 104238

Hewer F E (1998). Non-linear numerical model predictions of flow over an isolated hill of moderate slope. Boundary-Layer Meteorol, 87(3): 381–408

Hu P, Li Y, Han Y, Cai S C S, Xu X (2016). Numerical simulations of the mean wind speeds and turbulence intensities over simplified gorges using the sst k-ω turbulence model. Eng Appl Comput Fluid Mech, 10(1): 359–372

Huang G Q, Jiang Y, Peng LL, Solari G, Liao H L, Li M S (2019). Characteristics of intense winds in mountain area based on field measurement: focusing on thunderstorm winds. J Wind Eng Ind Aerodyn, 190: 166–182

Hunt J C R, Leibovich S, Richards K J (1988). Turbulent shear flows over low hills. Q J R Meteorol Soc, 114(484): 1435–1470

Iizuka S, Kondo H (2004). Performance of various sub-grid scale models in large-eddy simulations of turbulent flow over complex terrain. Atmos Environ, 38(40): 7083–7091

Ishihara T, Fujino Y, Hibi K (2001). A wind tunnel study of separated flow over a two-dimensional ridge and a circular hill. J Wind Eng Ind Aerodyn, 89: 573–576

Ishihara T, Hibi K (2002). Numerical study of turbulent wake flow behind a three-dimensional steep hill. Wind Struct, 5: 317–328

Ishihara T, Hibi K, Oikawa S (1999). Wind tunnel study of turbulent flow over a three-dimensional steep hill. J Wind Eng Ind Aerodyn, 83: 95–107

Jackson P S, Hunt J (1975). Turbulent wind flow over a low hill. Q J R Meteorol Soc, 101(430): 929–955

Kim H G, Lee C M, Lim H C, Kyong N H (1997). An experimental and numerical study on the flow over two-dimensional hills. J Wind Eng Ind Aerodyn, 66(1): 17–33

Kim J J, Baik J J, Chun H Y (2001). Two-dimensional numerical modeling of flow and dispersion in the presence of hill and buildings. J Wind Eng Ind Aerodyn, 89(10): 947–966

Kondo K, Tsuchiya M, Sanada S (2002). Evaluation of effect of micro-topography on design wind velocity. J Wind Eng Ind Aerodyn, 90(12–15): 1707–1718

Lilly D K (1992). A proposed modification of the Germano subgrid-scale closure method. Phys Fluids A Fluid Dyn, 4(3): 633–635

Liu Z, Ishihara T, Tanaka T, He X (2016). LES study of turbulent flow fields over a smooth 3-d hill and a smooth 2-d ridge. J Wind Eng Ind Aerodyn, 153: 1–12

Loureiro J B R, Alho A T P, Silva Freire A P (2008). The numerical computation of near-wall turbulent flow over a steep hill. J Wind Eng Ind Aerodyn, 96(5): 540–561

Mathey F Cokljat D, Bertoglio J P, Sergent E (2006). Assessment of the vortex method for large eddy simulation inlet conditions. Prog Comput Fluid Dy, 6(1–3): 58–67

Pearse J R, Lindley D, Stevenson D C (1981). Wind flow over ridges in simulated atmospheric boundary layers. Boundary-Layer Meteorol, 21(1): 77–92

Smagorinsky J (1963). General circulation experiments with the primitive equations. Mon Weather Rev, 91: 99–164

Sykes R I (1980). An asymptotic theory of incompressible turbulent boundary layer flow over a small hump. J Fluid Mech, 101(3): 647–670

Takahashi T, Ohtsu T, Yassin M F, Kato S, Murakami S (2002). Turbulence characteristics of wind over a hill with a rough surface. J Wind Eng Ind Aerodyn, 90(12–15): 1697–1706

Tamura T (2008). Towards practical use of LES in wind engineering. J Wind Eng Ind Aerodyn, 96(10–11): 1451–1471

Tamura T, Okuno A, Sugio Y (2007). LES analysis of turbulent boundary layer over 3D steep hill covered with vegetation. J Wind Eng Ind Aerodyn, 95: 1463–1475

Uchida T (2018). Large-eddy simulation and wind tunnel experiment of airflow over bolund hill. Open J Fluid Dyn, 8(1): 30–43

Wood N (2000). Wind flow over complex terrain: a historical perspective and the prospect for large-eddy modelling. Boundary-Layer Meteorol, 96(1–2): 11–32

Wood N, Mason P (1993). The pressure force induced by neutral, turbulent flow over hills. Q J R Meteorol Soc, 119(514): 1233–1267

Wurtele M G, Sharman R D, Datta A (1996). Atmospheric Lee Waves. Annu Rev Fluid Mech, 28(1): 429–476

Xu D, Taylor P A (1992). A non-linear extension of the mixed spectral finite difference model for neutrally stratified turbulent flow over topography. Boundary-Layer Meteorol, 59(1–2): 177–186

Yang Q S, Zhou T, Yan B W, Liu M, Van Phuc P, Shu Z R (2021). LES study of topographical effects of simplified 3D hills with different slopes on abl flows considering terrain exposure conditions. J Wind Eng Ind Aerodyn, 210: 104513

Yang Q S, Zhou T, Yan B W, Van Phuc P, Hu W C (2020). LES study of turbulent flow fields over hilly terrains – comparisons of inflow turbulence generation methods and sgs models. J Wind Eng Ind Aerodyn, 204: 104230

Yang Y, Gu M, Chen S Q, Jin X Y (2009). New inflow boundary conditions for modelling the neutral equilibrium atmospheric boundary layer in computational wind engineering. J Wind Eng Ind

Aerodyn, 97(2): 88–95

Yu Y, Yang Y, Xie Z (2018). A new inflow turbulence generator for large eddy simulation evaluation of wind effects on a standard high-rise building. Build Environ, 138: 300–313

Zheng D Q, Zhang A S, Gu M (2012). Improvement of inflow boundary condition in large eddy simulation of flow around tall building. Eng Appl Comput Fluid Mech, 6(4): 633–647

AUTHOR BIOGRAPHIES

Liang Li, received the B.S. degree in civil engineering from Henan University of Technology, Zhengzhou, China, in 2018, and the M.S. degree in structural engineering from Henan University of Technology, Zhengzhou, China, in 2021.

He is currently working toward the Ph.D. degree in civil engineering with School of Henan University of Technology, Zhengzhou, China. His research interests include computational fluid dynamics, especially in large eddy simulation of wind flow field around hilly terrains.

Email: 202191021@stu.haut.edu.cn.

Deqian Zheng, received the B.S. degree in civil engineering and the M.S. degree in structural engineering from Zhengzhou University, Zhengzhou, China, in 2003 and 2006, respectively, and got the Ph.D. degree in wind engineering from Tongji University, Shanghai, China, in 2011.

He is now working in the School of Civil Engineering as an Associate Professor of Henan University of Technology, and now he is Vice President. His research interests include computational fluid dynamics, especially in large eddy simulation of wind flow field around hilly terrains, wind environment, wind load and fluid structure interaction of building structures.

Dr. Zheng was Part-time Researcher Fellow of Wind Engineering Research Center at Tamkang University in 2017-2020. He got three second prizes for scientific and technological achievements of Henan Provincial Department of Education.

Email: deqianzheng@haut.edu.cn.